

1 MIMOC: A Global Monthly Isopycnal Upper-Ocean Climatology with Mixed Layers*

2

3 Sunke Schmidtko^{1,2}, Gregory C. Johnson¹, and John M. Lyman^{1,3}

4

5 ¹National Oceanic and Atmospheric Administration, Pacific Marine Environmental
6 Laboratory, Seattle, Washington

7 ²University of East Anglia, School of Environmental Sciences, Norwich, United
8 Kingdom

9 ³Joint Institute for Marine and Atmospheric Research, University of Hawaii at Manoa,
10 Honolulu, Hawaii

11

12 Accepted for publication in

13 *Journal of Geophysical Research - Oceans.*

14 Copyright 2013 American Geophysical Union. Further reproduction or electronic
15 distribution is not permitted.

16

17 8 February 2013

18

19

20 *Pacific Marine Environmental Laboratory Contribution Number 3805

21

22 Corresponding Author: Sunke Schmidtko, School of Environmental Sciences, University
23 of East Anglia, Norwich, NR4 7TJ, UK. Email: s.schmidtko@uea.ac.uk

Abstract

24

25

26 A Monthly, Isopycnal/Mixed-layer Ocean Climatology (MIMOC), global from 0–1950
27 dbar, is compared with other monthly ocean climatologies. All available quality-
28 controlled profiles of temperature (T) and salinity (S) versus pressure (P) collected by
29 conductivity-temperature-depth (CTD) instruments from the Argo Program, Ice-Tethered
30 Profilers, and archived in the World Ocean Database are used. MIMOC provides maps
31 of mixed layer properties (conservative temperature, Θ , Absolute Salinity, S_A , and
32 maximum P) as well as maps of interior ocean properties (Θ , S_A , and P) to 1950 dbar on
33 isopycnal surfaces. A third product merges the two onto a pressure grid spanning the
34 upper 1950 dbar, adding more familiar potential temperature (θ) and practical salinity (S)
35 maps. All maps are at monthly $\times 0.5^\circ \times 0.5^\circ$ resolution, spanning from 80°S to 90°N .
36 Objective mapping routines used and described here incorporate an isobath-following
37 component using a “Fast Marching” algorithm, as well as front-sharpening components
38 in both the mixed layer and on interior isopycnals. Recent data are emphasized in the
39 mapping. The goal is to compute a climatology that looks as much as possible like
40 synoptic surveys sampled circa 2007–2011 during all phases of the seasonal cycle,
41 minimizing transient eddy and wave signatures. MIMOC preserves a surface mixed
42 layer, minimizes both diapycnal and isopycnal smoothing of θ – S , as well as preserving
43 density structure in the vertical (pycnoclines and pycnostads) and the horizontal (fronts
44 and their associated currents). It is statically stable and resolves water-mass features,
45 fronts, and currents with a high level of detail and fidelity.

46

47 1 Introduction

48 An accurate description of the mean state of the ocean is a long-time goal of
49 oceanographic science. Global- to basin-scale surveys of ocean water properties were
50 initiated over a century ago, with the famous global expedition of the *Challenger* in the
51 1870s [Murray, 1885] followed by the *Fram* expedition towards the North Pole from
52 1893–1896 [Nansen, 1900], the *Discovery* expeditions to the Antarctic from 1924–1931
53 [Deacon, 1937], the *Meteor* expedition of the South Atlantic from 1925–1927 [e.g., *Wüst*
54 *and Defant*, 1936], the extensive Atlantic surveys associated with the International
55 Geophysical Year in 1957–1958 [e.g., *Fuglister*, 1960], the work on the *Eltanin* in the
56 Southern Ocean in the 1960s [e.g., *Gordon*, 1966; *Pytowicz*, 1968], and the global
57 GEOSECs survey during the 1970s [e.g., *Bainbridge*, 1976], to name several.

58 A recent and comparatively comprehensive milestone in global ocean water
59 property exploration was the one-time hydrographic survey conducted as part of the
60 international World Ocean Circulation Experiment (WOCE) during the 1980s and 1990s
61 [e.g., *King et al.*, 2001]. This monumental effort gathered measurements of a number of
62 different water properties with very high accuracy and high vertical and along-track
63 resolution from the ocean surface to its floor, with the global ocean sampled by a grid-
64 like pattern of coast-to-coast tracks. However, the effort, ship-time, and hence expense
65 required for such surveys necessitated gaps between tracks – and seasonal coverage was
66 largely lacking (most of the tracks were only visited once, usually not in winter – only a
67 few hardy scientists elect to work in, for instance, the Labrador Sea in February). Still,
68 this data set affords very useful three-dimensional information on ocean water properties,
69 and comprises a global baseline of late 20th century ocean conditions.

70 The Argo Program, with more than 3000 active, fully autonomous profiling floats
71 each collecting and reporting a CTD (conductivity-temperature-depth instrument) profile
72 between the surface and a target pressure of 2000 dbar, nominally every 10 days,
73 provides high-quality, spatially and temporally distributed sampling of temperature and
74 salinity in the global ice-free ocean [Roemmich *et al.*, 2009]. This program started in
75 2000, first achieved sparse global coverage by around 2004 or 2005, and reached its 3000
76 active float target in late 2007. Floats also now sample under seasonal sea ice [Klatt *et*
77 *al.*, 2007], and ice-tethered profilers (ITPs) [Toole *et al.*, 2011] provide data under
78 perennial Arctic sea ice. This near-global, year-round, high-quality sampling of the
79 upper half of the ocean volume for both temperature and salinity is revolutionary for
80 observational physical oceanography.

81 As oceanographic data have become more plentiful and better resolved, more
82 ocean climatologies and atlases have been constructed (e.g., Table 1). We compare our
83 results to three isobar-averaged global (or near-global) and monthly products: the World
84 Ocean Atlas 2009 [Locarnini *et al.*, 2010; Antonov *et al.*, 2010; hereafter WOA09], the
85 2009 CSIRO Atlas of the Regional Seas [Ridgway *et al.*, 2002; hereafter CARS09], and
86 the Argo-based Marine Atlas [Roemmich and Gilson, 2009; hereafter AMA]. WOA09 is
87 a monthly atlas mapped on isobars. CARS09, also an isobaric atlas, provides a mean,
88 annual, and semiannual harmonics, takes topography into account, and uses adaptive
89 smoothing scales. Both WOA09 and CARS09 use all available data to estimate a mean
90 seasonal cycle. Because of the irregular sampling of oceanographic data in the past, they
91 can be termed mixed-era climatologies. AMA uses Argo data only, and has monthly
92 maps for individual years starting in January 2004. Since the climatology presented here

93 also represents the mean seasonal cycle, for AMA we average all the years for a given
94 month prior to comparisons. Climatologies averaged on isopycnals also exist, but one is
95 solely a multi-year mean [*Gouretski and Koltermann, 2004*; hereafter WGHC] and
96 another is really a dataset and software tools [*Lozier et al., 1995*; *Curry, 1996*; hereafter
97 Hydrobase]. Hence we make a limited comparison of our results to WGHC and none to
98 Hydrobase.

99 Here we construct a global ocean climatology from 0–1950 dbar, the Monthly
100 Isopycnal/Mixed-layer Ocean Climatology (MIMOC), combining different features of
101 previous efforts and adding a few new features (Table 1). Interior ocean properties are
102 mapped on isopycnals, much like WGHC and Hydrobase, and those fields are provided.
103 However, we also map surface mixed layer properties, which are also provided. Finally,
104 we merge the mixed layer maps with those of the interior properties on isopycnals onto a
105 regular pressure grid.

106 We employ a topography-following mapping scheme, somewhat like CARS09,
107 but using a different algorithm, and add an equatorial latitudinal damping term to reflect
108 the more zonal hydrographic structures near the equator. We also include front-
109 sharpening weighting schemes within the ocean interior and in the mixed layer. Finally,
110 we focus on the best-sampled era, 2007–2011, where possible, supplemented by
111 historical CTD data. Historical data are given a lower signal-to-noise ratio to discount
112 them where sufficient recent data exist but to allow their use in the maps where recent
113 data are sparse, especially in some marginal seas, at high latitudes, and near the coasts
114 (including on continental shelves).

115 Immediately following this introduction, the data are discussed. Subsequently the
116 methods used to generate MIMOC are presented first in summary, and then individually
117 – motivated by targeted comparisons with other climatologies. After this presentation,
118 we discuss one area that could still benefit from improvement — joining the mixed layer
119 to the interior isopycnals in regions of strong gradients. Conclusions follow.

120 2 Data

121 This climatology uses CTD profiles from three sources: Argo floats [e.g. *Roemmich et*
122 *al.*, 2009], Ice Tethered Profilers [*Toole et al.*, 2011, hereafter ITPs], and shipboard data
123 from World Ocean Database 2009 [*Boyer et al.*, 2009; hereafter WOD]. Except in a few
124 isolated regions, Argo CTD data are the main data contributor in the open ocean and ITPs
125 are contemporaneous contributors in the Arctic (compare Fig. 1b and 1c). Since Argo
126 does not yet sample continental shelves, some marginal seas, or most ice-covered
127 regions, attempts to map the global oceans must include shipboard data. Since the
128 sampling periods of shipboard compared to Argo and ITPs are vastly different (Fig. 1a),
129 temporal sampling bias in mapping shelf regions and some marginal seas vs. the open
130 oceans is unavoidable.

131 All Argo float profiles from an Argo global data assembly center as of January
132 2012 that have a QC flag 2 or better are used, employing adjusted (delayed-mode)
133 variables as available (> 680,000 profiles, Fig. 1a, 1b). WOD CTD profiles available as
134 of January 2012 are used if quality flags are 0 or 2, profiles have monotonically
135 increasing pressure, at least 20 vertical measurements spaced less than 12 dbar apart, and
136 the maximum pressure is larger than the shallower of 200 dbar from the bottom or 1500
137 dbar (> 415,000 profiles, Fig. 1a, c). These last criteria are imposed to avoid introducing

138 biases or discontinuities in the maps that arise when combining numerous shallow
139 profiles (say to 1000 dbar, a common profiling pressure) with deeper ones, as discussed
140 in Section 3.1. Bathymetry data used for this quality control step and within the mapping
141 process in the following is the ETOPO-1 dataset [*Amante and Eakins, 2009*]. ITP
142 profiles processed to Level 3 as of May 2011 are used ($> 18,000$ profiles). For each week
143 of ITP data from each instrument, the median parameters on each isopycnal surface are
144 used to reduce the number of profiles, which are collected at higher than daily frequency.
145 No further quality control is applied to ITP data, since this data set is very well quality
146 controlled. In all instances, temperature (T) and salinity (S) must both be available at a
147 given reported pressure (P , or depth) level to be included (ITP profiles are included with
148 the Argo float data in Fig. 1).

149 While this basic, initial data screening benefits from the efforts of groups
150 involved with WOD, Argo, and ITP, it might be deemed minimal compared to the
151 rigorous, labor-intensive visual quality control effort applied to the datasets for some
152 climatologies, e.g., Hydrobase. Our quality control relies instead on a robust mapping
153 algorithm including the removal of outliers via statistical filters and automatic down-
154 weighting of data points with unusual water-mass properties that pass through these
155 filters.

156 3 Methods: Constructing the climatology

157 Constructing MIMOC is fairly involved, so we outline the process here before delving
158 into detail. First, the profiles are prepared, with water properties derived and interpolated
159 onto isopycnal surfaces. We compute properties of the mixed layer using the density
160 algorithm of *Holte and Talley* [2009]. Then data near each gridpoint are selected and

161 outliers are found and discarded as detailed below. Distance from the grid-point includes
162 consideration of fronts (data on the other sides of fronts are considered farther away) and
163 bathymetry (along-isobath distances are considered closer than across-isobath distances
164 using a fast-marching algorithm, and land barriers are respected). Mean properties
165 weighted by distance are generated as a first guess prior to objective mapping. Pre-2007
166 data are de-emphasized in the objective maps by increasing their noise-to-signal energy
167 in the mapping. Objective maps of water properties in the mixed layer and on isopycnals
168 in the ocean interior are generated. These maps are lightly low-pass filtered and gaps are
169 filled. Spice-preserving adjustments are made to Θ and S_A to compensate for effects of
170 artificial mixing (smoothing) in the presence of a non-linear equation of state. The mixed
171 layer and interior isopycnal maps, both products themselves, are also merged onto a set of
172 standard pressures to make a third product.

173 *3.1 Profile preparation*

174 For each individual profile, conservative temperature, Θ , absolute salinity, S_A , and
175 surface-referenced potential density anomaly, σ_0 , are calculated using v3.0 of the 2010
176 TEOS equation of state [IOC, SCOR and IAPSO, 2010; McDougall et al., in preparation].
177 Neutral density, γ_n , cannot be used in the construction, since the climatology is global,
178 including marginal seas where neutral density is not defined [McDougall and Jackett,
179 2005]. The mixed layer S_A , Θ , σ_0 , and depth (hereafter mixed layer pressure, MLP , since
180 pressure is used here as the vertical coordinate) are computed using the Holte and Talley
181 [2009] density algorithm. If the algorithm fails to provide a MLP (e.g., when $P > 20$ dbar
182 for the shallowest measurement) the profile is removed from the data set.

183 As a quality control measure any profiles with density inversions $> 0.06 \text{ kg m}^{-3}$
184 between two vertically adjacent measurements are discarded. This threshold is twice the
185 Argo real-time quality control test for inversions. These relatively small density
186 inversions are tolerable and assumed to originate from measurement inaccuracies or
187 truncation errors. Of the 680,000 float profiles that pass QC, 470,000 have inversions $<$
188 0.06 kg m^{-3} . These are mitigated by re-ordering raw profiles by density.

189 Following these steps, S_A , Θ , and P for each profile are linearly interpolated
190 vertically onto 550 fixed σ_0 surfaces, without extrapolation. The surfaces chosen are a
191 compromise between reasonable computation time and file sizes versus adequate vertical
192 resolution throughout the global ocean and marginal seas, with their large regional
193 variations in vertical distribution of σ_0 . The first 389 isopycnal surfaces are distributed in
194 9 linear subsets with decreasing σ_0 intervals from $-1 \leq \sigma_0 \leq 27.938 \text{ kg m}^{-3}$. The last 161
195 isopycnals in four subsets are again linearly spaced from $27.94 \leq \sigma_0 \leq 29.44 \text{ kg m}^{-3}$, but
196 with varying σ_0 intervals to span the dense waters in the Nordic and Mediterranean seas.

197 Where isopycnals outcrop at the surface or at the bottom, the mapping algorithm
198 only has data on one side, spatially or temporally. For isobaric mapping this problem is
199 limited to near bathymetry. This situation leads to maps biased towards interior ocean
200 values close to the surface and the bottom.

201 To overcome this bias at the surface, profiles with denser mixed layers are
202 extended with lighter isopycnal values at pressure 0. Here Θ and S_A are filled with
203 LOWESS-mapped (robust LOcally Weighted regrESSion; Cleveland 1981) Θ and S_A
204 using the closest 30 profiles in density space on either side of the isopycnal being filled.
205 The LOWESS maps fit a mean as well as a plane in density, seasonal-time, virtual

206 latitude and virtual longitude. The weights used are those used for computing the
207 respective monthly mixed layer for the grid point, but with a floor set at 0.05 to ensure
208 the plane fitting is not overly influenced by spatiotemporally close but variable data.
209 This method prevents isopycnals directly below the mixed layer from being mapped
210 based on data from the ocean interior alone and allows isopycnal mapping up to the
211 mixed layer, without switching to isobaric mapping in the upper ocean as done in other
212 isopycnal climatologies such as the WGHC, that uses isobaric mapping for the upper 100
213 dbar.

214 At our maximum mapping pressure of 1950 dbar Argo floats sporadically sample
215 higher densities due to internal waves, leading to a bias towards shallower pressure
216 values in the isopycnal maps. Fronts at this depth are not as pronounced as at the surface,
217 thus we use a simple objective mapping to make a best guess Θ and S_A approximation. P
218 is extrapolated by using the weighted mean $\Delta P/\Delta\sigma_\theta$ from profiles reaching deeper, using
219 the identical weights as for the main MIMOC computation discussed below, but without
220 the temporal term. For Θ and S_A , data are handled similarly to the final mapping
221 described below; with statistical outliers removed in S_A , P and Θ , a front-finding
222 algorithm in P applied and weighted means of the data used as first guess for the
223 objective maps. Finally objective mapping is performed with the same decadal down-
224 weighting with noise as detailed below. P is not extended vertically in the same step as Θ
225 and S_A since $\Delta P/\Delta\sigma_\theta$ requires the next denser isopycnal to be available in a profile as well,
226 so doing so would further limit the data available for Θ and S_A .

227 3.2 Data selection and objective mapping

228 All objective maps are global from the Antarctic shelf to the North Pole and made at
229 monthly $\times 0.5^\circ \times 0.5^\circ$ lateral resolution, covering all areas with water depth $> 10\text{m}$
230 according to ETOPO-1. The objective mapping procedure used is standard [e.g.,
231 *Bretherton et al.* 1976], but with three innovations, each explained in subsections that
232 follow. One innovation is the use of a fast-marching algorithm to transform distance
233 coordinates based on the bottom topography and the presence of the equator, reducing
234 smoothing across isobaths and the equator, and preventing smoothing across land. This
235 innovation is foreshadowed immediately below by the term “along-pathway distance”. A
236 second innovation is additions to the weighting and covariance functions that sharpen
237 fronts in both the mixed layer and the ocean interior, also explained later. A third
238 innovation is an addition to the diagonal of the covariance matrix that de-emphasizes data
239 prior to 2007 in the objective maps.

240 For the mixed layer we map σ_0 , Θ , S_A , MLP , year values, and a formal error. On
241 σ_0 surfaces in the ocean interior we map Θ , S_A , P , σ_0 , year, and formal error. In addition,
242 we also iteratively generate weighted means, as described below, for all these quantities.
243 These weighted means are used as first-guesses for the objective maps and are
244 comparatively smooth. They may be useful for work that requires that characteristic. For
245 the mixed layer and pressure-gridded products we compute potential temperature, θ , and
246 practical salinity, S , from Θ , S_A .

247 The closest 2250 profiles within 2000 km of the along-path distance from each
248 gridpoint (regardless of month) are used for mapping at that gridpoint. If there are less
249 than 2250 profiles in this radius, then all are used, but data from more than five profiles

250 must be found to attempt a map for a gridpoint. If five or fewer profiles are available for
 251 a grid point, it is ignored in the objective mapping but filled by lateral interpolation (or
 252 extrapolation) when constructing the final products as detailed below. The initial
 253 weighting function (accounting for along-path distance and time of the year) is assigned a
 254 conventional Gaussian form:

$$255 \quad w_i = \exp \left\{ - \left[\left(\frac{\Delta t}{L_t} \right)^2 + \left(\frac{\Delta d_x}{L_x} \right)^2 \right] \right\}, \quad (1)$$

256 where Δt is the temporal difference between the month being mapped and that of the data
 257 value (circular, disregarding the year), L_t the temporal decorrelation scale of 45 days, Δd_x
 258 the along-path distance between the gridpoint and the data sample, and L_x the lateral
 259 decorrelation scale of 330 km.

260 For each month the 300 profiles with the highest weights and 200 more random
 261 profiles from the next highest-weighted 1500 profiles are selected from the 2250 points
 262 mentioned above. The number of data points used and their selection method are
 263 compromises that balance available computational time and accurate mapping; they
 264 provide sufficient data for the mapping algorithm to map the local properties and their
 265 gradients in the larger area. A floor of $\varepsilon = 10^{-6}$ is set for a new, modified weighting
 266 function, $W_i = w_i \cdot (1 - \varepsilon) + \varepsilon$. This floor mitigates problems that arise from rounding
 267 errors.

268 *3.3 Removing outliers*

269 Prior to computing the maps we discard outliers using an interquartile range (IQR) filter.
 270 The IQR is simply the third minus the first quartile. Here outliers are defined as being
 271 more than twice the IQR below the first quartile or more than twice the IQR above the

272 third quartile. This cut-off is analogous to retaining data within 2.7 standard deviations
 273 on either side of the mean, or > 99.9% of the data, for a normal distribution. In the mixed
 274 layer this filter is applied to σ_0 and MLP values. On interior isopycnals this filter is
 275 applied to P and S_A . Since S_A and Θ are very highly correlated on isopycnals, application
 276 of the filter to Θ would be redundant.

277 *3.4 Sharpening fronts and downweighting remaining outliers*

278 One modification to the weighting and covariance functions prior to mapping the data is
 279 designed to sharpen fronts. For the mixed layer the weighted standard deviation for S_A
 280 and Θ are computed and used in a term added to the weighting and covariance functions
 281 so

$$282 \quad \omega_i = \exp \left\{ - \left[\left(\frac{\Delta t}{L_t} \right)^2 + \left(\frac{\Delta d_x}{L_x} \right)^2 + \left(\frac{\Delta S_A}{1.2 \cdot \sigma_{S_A}} \right)^2 + \left(\frac{\Delta \Theta}{1.2 \cdot \sigma_{\Theta}} \right)^2 \right] \right\}, \quad (2)$$

283 where $\Delta \Theta$ is the difference between the each observed Θ and the locally weighted mean
 284 Θ calculated using the weight vector \mathbf{W} with the weights \mathbf{W}_i , ΔS_A is defined analogously.
 285 As above, a floor of 10^{-6} is set for all elements of ω_i and the result is used to compute a
 286 local weighted mean at each gridpoint for all of the properties to be mapped (including
 287 σ_0). This algorithm sharpens density fronts in the mixed layer. The factor of 1.2 is
 288 chosen to optimize the results based on visual examination of differences between the
 289 mixed-layer mapping and the uppermost mapped isopycnal. These weights are then used
 290 to re-compute the local weighted mean in S_A and Θ , which are thereafter used in the
 291 above equation for ω_i to compute the final set of weights.

292 The advantage of using Θ and S_A rather than σ_0 for front sharpening in the mixed
 293 layer is to resolve thermal and haline gradients that are density compensated as they are

294 within the mixed layer in many ocean regions [e.g., *Rudnick and Ferrari, 1999*].
295 Furthermore, *MLP* is not suitable for mixed-layer front detection since it often exhibits
296 very large and non-normal variability on short temporal and spatial scales.

297 On σ_0 surfaces, we use P for a single front-sharpening parameter, otherwise
298 analogous to the procedure above. This is a dynamical front detector, sensitive to the
299 large vertical excursions of P on σ_0 across strong currents like the Gulf Stream, Kuroshio
300 Extension, and Antarctic Circumpolar Current. This modification to the weighting and
301 covariance functions tends to sharpen θ , S , and P gradients across these fronts,
302 suppressing artificial mixing of water masses, and making the mapped fields look more
303 like a synoptic survey, which will generally find sharp fronts and strong currents.
304 Furthermore, using P for front sharpening on σ_0 surfaces reduces the weight of any
305 erroneous measurement in Θ , S_A , or P . The resulting strong interior gradients are clear
306 from meridional sections (e.g., in the western South Atlantic, Fig. 2) crossing the
307 Antarctic Circumpolar Current (here near 50°S) and the subtropical front (near 40°S). In
308 these locations, especially at the subtropical front, the meridional water property
309 gradients in each of the other climatologies are much smoother than those in MIMOC,
310 resulting in dipoles of water property anomalies of these climatologies with respect to
311 MIMOC, especially pronounced at mid-depth, from 200–600 dbar around the subtropical
312 front. Synoptic meridional sections in this region [e.g., Fig. 2a, b; *Tsuchiya et al., 1994*]
313 look much more like MIMOC in the strength of these fronts than do the other
314 climatologies, except the synoptic sections also contain prominent eddies that MIMOC
315 does not retain.

316 *3.5 Covariance matrix and de-emphasizing pre-2007 data*

317 In addition to providing weighted means that are used as the first guess for the objective
 318 maps, the equations above are used to construct the covariance matrices for the objective
 319 maps, like the following for the mixed layer:

$$320 \quad E_{ij} = \exp \left\{ - \left[\left(\frac{\Delta t}{L_t} \right)^2 + \left(\frac{\Delta d_x}{L_x} \right)^2 + \left(\frac{\Delta S_A}{1.2 \cdot \sigma_{S_A}} \right)^2 + \left(\frac{\Delta \Theta}{1.2 \cdot \sigma_{\Theta}} \right)^2 \right] \right\}. \quad (3)$$

321

322 On isopycnals the last two terms in (3) are replaced with $[|\Delta P| / (1.2 \cdot \sigma_P)]^2$, thus instead
 323 of a Gaussian weighting by Θ and S_A , only a Gaussian weighting by P is used. The
 324 difference between the weighting and the covariance matrices is as follows: In the
 325 former the numerators of the three terms in the Gaussian are the differences between each
 326 parameter and the grid-point time, location, and weighted mean front-sharpening
 327 parameter (Θ and S_A for the mixed layer and P for σ_0 surfaces in the ocean interior). In
 328 the latter the numerators are the difference in each parameter between the profiles i and j .

329 An estimate of noise-to-signal ratio is typically added to the diagonal of the
 330 covariance matrix prior to objective mapping. Here we use the form:

$$331 \quad E_{ii} = E_{ii} + \kappa_0 + \kappa_{decade} \cdot \left\{ 1 - \exp \left[- \left(\frac{\Delta yr}{\tau} \right)^2 \right] \right\}, \quad (4)$$

332 where E_{ii} is the diagonal of the covariance matrix \mathbf{E} and κ_0 is a constant noise-signal
 333 ratio, set here to 1.5. This value is chosen, again, by visual evaluation of test cases; this
 334 time optimizing between smoothness and feature resolution. Here our innovation is to
 335 use the noise to de-emphasize pre-2007 data in the objective maps. We set κ_{decade} to 8.5
 336 years and Δyr is the number of years prior to 1 January 2007 for each data point. After

337 that date Δyr is set to 0. The time-scale τ is set to 12 years. This formulation for the
338 noise ensures that the objective maps are for modern conditions wherever modern data
339 are available. However, the weighted means (which are used as the first-guess for the
340 map and to which the map relaxes in data-sparse regions) are a mixed-era average that
341 includes historical CTD data (dating back to 1970). To make full use of the capabilities of
342 objective mapping in the absence of recent data (since 2007) we set a floor of 1.5 for the
343 noise-to-signal ratio. This floor ensures that in the sole presence of historic data
344 objective mapping does not relax towards the weighted mean too strongly.

345 The influence of a modern climatology is apparent in areas which have undergone
346 changes in water-mass properties in recent decades, like the warming and shoaling of
347 intermediate water masses [e.g., *Schmidtko and Johnson, 2012*]. Weighting historical
348 data in MIMOC less than in climatologies like CARS09 or WOA09 leads to warmer
349 temperatures at 500 dbar in MIMOC, especially in areas with abundant historic profiles,
350 since MIMOC represents the modern state of the ocean rather than that of prior decades
351 (Fig. 1b–c; 3c–d). AMA on the other hand, using only Argo data after 2004, is as warm
352 or even warmer than MIMOC (Fig. 3b). Shelf regions and high latitude regions with no
353 ITP data lack the amount of recent data provided in the open ocean by Argo, thus are
354 more representative of the state of the ocean before 2000 in MIMOC. MIMOC mapped
355 years are available as an indicator of the local "vintage" of maps.

356 At this point objective mapping, also known as optimal interpolation, objective
357 interpolation or objective analysis, $b = \omega \cdot E^{-1} \cdot \psi$, is performed on the anomalies of each
358 parameter from its weighted mean. The spatial correlation scales and signal-to-noise
359 levels used in constructing MIMOC maps are not determined from the data but

360 prescribed, adding a subjective element to this procedure. Nonetheless, we refer to this
 361 operation as objective mapping hereafter. Here ψ is the vector of residuals of the
 362 measured properties and the weighted means, and b is the objectively mapped anomaly.
 363 Values of the mapped properties are computed by adding the weighted means to the
 364 objectively mapped anomalies b . Formal errors are also estimated for the objective maps.

365 *3.6 Fast-Marching: Taking bathymetry and the equator into account*

366 In the ocean near-conservation of potential vorticity [e.g., *Pedlosky*, 1987] means that
 367 along-isobath decorrelation scales are much longer than cross-isobath ones, and
 368 especially in low latitudes, zonal decorrelation scales are much longer than meridional
 369 ones. Ocean currents also respect coastlines, with no flow into land. We construct an
 370 along-pathway distance to reflect the above constraints using the fast marching method
 371 [*Sethian*, 1996, 1999], which is based on *Dijkstra's* [1959] algorithm. This method is
 372 often described in terms of wave-front propagation, as it solves the boundary value
 373 problem of the Eikonal equation, $SM_i |\nabla t_i| = 1$, where t is the time and SM_i is the speed at
 374 each location in the normal direction of propagation. Hereafter SM is called the speed
 375 map. Here it is defined between 0 and 1 and represents the fraction of normal
 376 propagation speed. Thus 0 effectively halts wave-front propagation at a gridpoint and 1
 377 allows normal speed wave-front propagation through a gridpoint.

378 However, here we are really more interested in adjusting distances, so the time to
 379 reach gridpoints from the origin, the gridpoint being mapped, is here re-interpreted as
 380 distance. We determine a spatially varying speed map for each gridpoint being mapped
 381 with the form:

$$382 \quad SM_i = \left[1 - \left| \log \left(\frac{H_0}{H_i} \right) \right| \right] \cdot \exp \left[\frac{\vartheta_0 - \vartheta_i}{\exp \left(\frac{\vartheta_0}{7.5} \right)} \right], \quad (5)$$

383 where H_0 is the water depth at the gridpoint being mapped, H_i are the water depths in
 384 nearby grid boxes i in which data points might be located, ϑ_0 is the latitude of the
 385 gridpoint being mapped, and ϑ_i are the latitudes of nearby grid boxes i . The depth for
 386 each gridpoint is determined by the median of all depths within the area of the grid box in
 387 the ETOPO1 dataset. If more than two-thirds of the area associated with a grid box is
 388 above the surface, the whole gridpoint is treated as land to ensure narrow passages are
 389 closed to the mapping. Since (5) is very sensitive to changes in shallow water, H_0 and H_i
 390 are set to a floor of 75 m, which leads to a less sensitive speed map on the shelf.

391 The speed map is unity in locations that have the identical depth and same latitude
 392 as the gridpoint to be mapped. The logarithmic term in (5) reduces the traveling speed
 393 through grid boxes with significant differences in water depth from the gridpoint being
 394 mapped. The exponential term reduces the speed through grid boxes that are at different
 395 latitudes than any gridpoint being mapped. The closer to the equator the gridpoint being
 396 mapped, the stronger is this effect. Thus the first term creates a longer along-path
 397 distance than the Cartesian one for cross-isobath mapping, while the second term creates
 398 a longer distance than the Cartesian one for meridional mapping, more anisotropic nearer
 399 the equator. We set a floor of $SM_i = 0.05$ for any water-covered area, a maximum
 400 twenty-fold increase in path distance. However, $SM = 0$ for gridpoints marked as land to
 401 prevent mapping pathways from crossing land. Hence fast marching eliminates the

402 necessity to define "hand-drawn" boundaries for mapping around peninsulas, basin
403 boundaries, bays and such.

404 The fast-marching algorithm does not retain the second dimension, but that
405 information is necessary for objective mapping of fields with spatial gradients. Hence we
406 determine the angles at which the fast-marching pathways must leave each gridpoint
407 being mapped to reach each fast-marching grid box via the minimum fast-marching
408 distance. These angles are then applied to the data along with the fast-marching distances
409 to effect a complete transformation from geographic to fast-marching coordinates.

410 The effectiveness of fast marching in separating ocean interior from shelf waters
411 is well illustrated in the Bering Sea (Fig. 4), where the Bering Slope Current [e.g.,
412 *Johnson et al.*, 2004] is associated with a front between the interior ocean and the Bering
413 Shelf. Here MIMOC (Fig. 4a, b) exhibits a distinct separation of cold, fresh shelf waters
414 and warmer, saltier waters offshore that is blurred in some other climatologies (Fig. 4c–
415 f). Also, in the southern half of the Bering Shelf, just as in synoptic sections [e.g.,
416 *Coachman*, 1986], MIMOC has the strongest S gradient located right at the shelf break,
417 and the strongest θ gradient slightly northeast (landward) of the shelf break.

418 *3.7 Post-mapping – smoothing and infill.*

419 Mapped values at grid points with weight $< 10^{-6}$ are removed to eliminate any remaining
420 artifacts associated from round-off errors. After discarding these points from the maps,
421 water properties in the mixed layer and on each interior ocean isopycnal surface are
422 smoothed with a two-dimensional 5th-order binomial filter to reduce small-scale noise.
423 This noise, likely owing to the fast-marching algorithm, is on the order of $\pm 0.05^\circ\text{C}$ in
424 mixed layer temperatures and $< \pm 0.01^\circ\text{C}$ at pressures > 900 dbar. Water properties are

425 also interpolated (and extrapolated) onto missing gridpoints with a spatial 3rd-order
426 binomial filter. These steps are performed iteratively, always smoothing or filling
427 locations with a maximum of adjacent gridpoints first.

428 3.8 Cabbeling biases

429 Because of the non-linearity of the equation of state, waters of the same density and
430 pressure but different Θ and S_A (warmer-saltier versus colder-fresher) will always become
431 slightly denser when mixed, a process called cabbeling [McDougall, 1987]. This process
432 can create biases in density when mapping, because mapping explicitly smooths (hence
433 artificially mixes) Θ and S_A data [e.g., Gille, 2004]. The result is that densities are
434 generally greater (and sea level lower) when they are computed from mapped values
435 rather than mapped themselves.

436 The MIMOC fast-marching and front-sharpening algorithms minimize smoothing
437 of distinct water-masses, but smoothing is part of constructing a climatology, and in
438 regions of strong fronts, the non-linear mixing biases become noticeable. They are
439 especially apparent when mapping on isopycnals because the density calculated from
440 mapped Θ and S_A values on an isopycnal is different (usually denser) than the initial
441 isopycnal, especially in regions of strong Θ - S_A gradients (Fig. 5).

442 There are two possible responses to this problem: One can choose to conserve θ
443 and S and accept any (largely localized) increase in density, or one can adjust the mapped
444 θ and S values so they lie back on the initial isopycnal and conserve density. While
445 conservation arguments support the former course, this is an isopycnal climatology, so
446 we choose the latter. We further choose to conserve spiciness [e.g., Flament, 2002] in
447 our adjustment, meaning that we make the water properties warmer and fresher in

448 amounts so that Θ and S_A changes contribute equally in terms of their contributions to
 449 density for the return to the initial isopycnal. Thus additive adjustments $\Delta\Theta$ and ΔS_A are
 450 given by

$$451 \quad \Delta\Theta = \frac{\sigma_0(S_{Amap}, \Theta_{map}) - \sigma_{0i}}{2\alpha\rho_0} \quad \text{and} \quad \Delta S_A = \frac{\sigma_0(S_{Amap}, \Theta_{map}) - \sigma_{0i}}{2\beta\rho_0}, \quad (6)$$

452 where σ_{0i} is the initial isopycnal, Θ_{map} and S_{Amap} the properties mapped, α the local
 453 thermal expansion coefficient, and β the local haline contraction coefficient (Fig. 5). The
 454 adjustments are everywhere sufficiently small that the local tangent to density (lines of
 455 constant spice) can be linearized. To be consistent we make similar adjustments to Θ and
 456 S_A for the mixed layer maps, using the mapped mixed layer density as a target for the
 457 adjustments.

458 Some of the strongest non-linear mixing biases found are in the western boundary
 459 currents and their extensions – where the warm salty waters of the subtropical gyres
 460 collide with the waters of the colder and fresher subpolar gyres. The North Atlantic
 461 Current is an extreme example (Fig. 6). Even in the highest gradient regions of the upper
 462 reaches of this current between the gyres the adjustments only reach about +0.5 °C for Θ
 463 and about -0.1 for S_A (up to +1.1 °C and -0.16 PSS-78 on isolated gridpoints). If these
 464 biases were left in density, isopycnals in the core of the current would artificially shift
 465 about 20 km northward in the upper 80 dbar of this same region. More generally these
 466 biases are quite small. The median correction for Θ is 1.0×10^{-3} °C on isopycnals. The
 467 median correction for Θ in the mixed layer (1.1×10^{-3} °C) is only slightly larger.

468 3.9 Back to pressure co-ordinates: Connecting the mixed layer and interior isopycnal
469 maps.

470 Monthly maps of water properties in the mixed layer and on interior ocean isopycnals are
471 products in their own right, but we also combine them onto a regular pressure grid for
472 increased ease of use. This re-gridding is done at each geographical grid-point and for
473 each month. Mixed layer properties are assigned to all pressure grid-points shallower
474 than the local *MLP*. The *MLP* and interior ocean pressures at least 5dbar greater than the
475 *MLP* and lower than the maximum possible bottom pressure are used to put θ and S on a
476 regular pressure grid via linear interpolation.

477 4 Discussion

478 One advantage of isobaric mapping is that it is simple and can be performed over the
479 whole water column. In contrast, isopycnal mapping requires the separate computation
480 of the mixed layer, or a surface isobaric layer, for the reasons detailed below. This
481 calculation can either be done by isobaric mapping down to a depth generally below the
482 seasonal thermocline (e.g., WGHC), or by merging an separately mapped mixed layer to
483 the interior ocean isopycnal maps, as done here. The isopycnal/mixed-layer formulation
484 has some very significant advantages over a simple isobaric mapping, for example
485 following water-masses in the vertical, preserving vertical stratification, and enforcing
486 hydrostatic stability (at least for the density parameter used to construct the climatology,
487 in this case σ_0). The additions of front-sharpening and bathymetry-respecting algorithms
488 add to those advantages. However, there are always trade-offs in constructing a
489 climatology. One difficulty – biases in density resulting from artificial cabbeling owing

490 to smoothing during the mapping process – has been previously recognized [e.g., Lozier
491 et al. 1994; 1995], and discussed and dealt with above. In fact, that issue is probably
492 larger in most isobaric climatologies, although efforts have been made to mitigate the
493 artifacts [Locarnini et al., 2009; Antonov et al., 2009]. A remaining issue that merits
494 further improvements, the difficulty of mapping near regions where isopycnals outcrop,
495 is discussed at the end of this section.

496 *4.1 Mixed layer*

497 A mixed layer is often a desirable feature in a climatology. The mixed layer is in direct
498 contact with the atmosphere and water properties are by definition homogeneous there (in
499 the ocean and in MIMOC, e.g., Fig. 7). Resolving the seasonal cycle in the mixed layer,
500 including dense, deep winter mixed layers, is crucial to water mass formation [e.g.
501 *Stommel, 1979*]. Thus resolving the mixed layer and its temporal evolution in a
502 climatology better allows study of water mass formation using that climatology. For
503 example, the evolution of a deep winter mixed layer is clear in MIMOC (Fig. 7) within
504 the formation regions for the South East Pacific Subtropical Mode Water (SEPSTMW) at
505 20.5 °S and 99.5 °W, as expected from analyses of synoptic data [e.g., *Wong and*
506 *Johnson, 2003*], but is less obvious in other climatologies (Fig. 7). A global comparison
507 of MIMOC maximum mixed layer depths with other commonly used mixed layer depths
508 (Fig. 8) shows MIMOC with sharper gradients between areas with deep and shallow
509 maximum mixed layer within the course of the year. The mixed layer is also clear in
510 vertical sections from synoptic data and MIMOC, but again less clearly defined in other
511 climatologies (Fig. 2).

512 4.2 Isopycnal mapping

513 Isopycnal maps better follow water parcels both laterally and vertically. One advantage
514 of this tendency over isobaric maps is limiting the creation of artificial water masses
515 found in climatologies smoothed on isobars [e.g., *Lozier et al.*, 1994]. The smoothing
516 effects on vertical density gradients by transient vertical excursions of isopycnals owing
517 to planetary waves, internal waves, and tides are also greatly reduced in isopycnal maps
518 relative to isobaric maps.

519 For example, the strong and shallow pycnocline in the eastern equatorial Pacific
520 undergoes substantial excursions owing to the seasonal cycle [e.g., *Johnson et al.*, 2002],
521 but also from Kelvin waves, Rossby waves, and ENSO [e.g., *McPhaden and Yu*, 1999].
522 In an isobaric average these vertical excursions of isopycnals (along with those owing to
523 eddies, internal waves, and tides) will tend to smear out the pycnocline in the vertical and
524 reduce its magnitude substantially from what would be observed in a synoptic survey, as
525 well as reducing the magnitude of $\Theta-S_A$ features within the pycnocline. As a result,
526 MIMOC exhibits a much stronger and sharper pycnocline in this region than do other
527 climatologies (as visualized by the squared Brunt-Väisälä frequency $-N^2$; Fig. 9, right
528 panels), and much better preserves the South Pacific salinity maximum and North Pacific
529 salinity minimum that meet within the pycnocline at the equator [Fig. 9, left panels; e.g.,
530 *Johnson and McPhaden*, 1999].

531 4.3 Isopycnal boundary problems

532 One aforementioned problematic issue with isopycnal mapping is that mapping errors
533 which increase near the boundaries of the domain, where data are only available on one
534 side of the mapped gridpoint, occur not only near coastlines and at the edges of data-

535 sparse regions as they do for other maps, but also anywhere (or anytime) that the
536 isopycnal outcrops in the ocean interior. On the other hand, the mixed layer (and any
537 isobaric) maps do not have this source of uncertainty (and bias) in the ocean interior.

538 Biases from this isopycnal mapping uncertainty should be most noticeable where
539 the mixed layer meets interior ocean isopycnals in regions with large surface density
540 gradients and limited data availability, for instance in the Antarctic Circumpolar Current
541 (Fig. 10). The temperature inversion visible in MIMOC just below the mixed layer here
542 may occur at least in part because the mixed layer map is constrained by both the colder,
543 fresher water to the south and the warmer saltier water to the north, whereas the isopycnal
544 maps near their surface outcrops would mostly (except for the upward profile extensions
545 described above) see the warmer, saltier water to the north of the outcrop. Thus, the
546 isopycnal maps could be biased towards those northern warm salty values, potentially
547 creating the temperature inversion just below the mixed layer visible here, or small
548 discontinuities between the mixed layer and the ocean interior seen in other locations.
549 This feature has been largely mitigated by the upward profile extension, but is not
550 completely resolved. However, what remains may also be realistic; some of the raw
551 profiles in the region do display a temperature inversion similar to that found in the maps.

552 A similar problem is found on dense isopycnals near 1800–2000 dbar, where the
553 majority of data profiles used here end. In this instance the densest isopycnals are
554 observed by Argo only when they are shallower than average, whereas slightly lighter
555 isopycnals are observed for their entire pressure range. Hence, the densest isopycnals are
556 biased towards shallow pressures in the maps, creating artificially strong stratification
557 just above 2000 dbar. Again the extension described above reduces the impact of sudden

558 drops in data density, but close to bottom of the mapping ranges values may be biased
559 towards shallower depths and properties. For this reason MIMOC is only published up to
560 1950 dbar where this problem is still limited. To include the deeper oceans, MIMOC
561 would need to be recomputed with full-depth CTD profiles only and then merged to the
562 upper ocean climatology. While we plan to effect this improvement, it is not a simple
563 task, because a new problem of temporal discontinuities in full depth vs. upper ocean
564 sampling arises.

565 5 Summary

566 MIMOC is a monthly isopycnal/mixed-layer ocean climatology with three products: 1.
567 Mapped mixed layer properties (S and θ , or S_A and Θ with MLP). 2. Mapped water
568 properties (S and θ or S_A and Θ with P) on selected potential density surfaces. 3. Water
569 properties (S and θ or S_A and Θ) from the first two products merged onto a regular
570 pressure grid. Numbers of weighted observations for the maps, the mapped dates, and
571 formal mapping errors are provided for the mixed layer and isopycnal maps. The
572 numbers of weighted observations for the maps and the mapped dates are also provided
573 for the maps on the pressure grid. Smoother weighted-mean fields are also provided.

574 The goal of MIMOC is to make maps that preserve many of the features observed
575 in a synoptic survey, but minimizing the influences of eddies, planetary waves, internal
576 waves and tides, and other transient phenomena. MIMOC preserves water-mass
577 properties both vertically and laterally; resolves boundary currents and shelf regimes
578 (where data are available) while observing natural boundaries like land, inlets, islands,
579 and ridges; accounts for the short meridional scales of the equatorial current systems;

580 retains true mixed layers as well as preserving strong, sharp pycnoclines; and is stably
581 stratified.

582 To accomplish these goals MIMOC uses mapping mechanisms including
583 combining mixed layer and interior isopycnal maps, employing front-sharpening
584 algorithms that down-weight profiles with regionally atypical characteristics, and a “Fast
585 Marching” algorithm that accounts for the influences of bathymetry and latitude
586 (especially near the equator) on water-property distributions. Comparing MIMOC in
587 detail to other widely used climatologies suggests that MIMOC fulfills the goals listed
588 above as well as or better than any of the comparison products.

589 Isopycnal maps are more uncertain, and perhaps even biased, near their surface
590 outcrops, so joining the ocean interior to the surface mixed layer in MIMOC is not free
591 from difficulty, especially in regions of large surface density gradients and sparse data
592 distributions. However, procedures are applied that largely mitigate this problem and a
593 similar one near the bottom of the climatology. Residual mismatches may still result in
594 small temperature inversions or other discontinuities.

595 MIMOC could not be constructed without a high-quality, temporally and spatially
596 well-sampled set of profiles of contemporaneously measured temperature and salinity –
597 Argo. Improvements could include extending MIMOC to the deep ocean, adding data in
598 remote regions, mapping water-mass properties additional to S_A and Θ (or S and θ), and
599 developing a more sophisticated method for matching mixed layer and isopycnal
600 properties at outcrop locations.

601

602 Appendix: Data Access

603 The climatology is currently hosted at <http://www.pmel.noaa.gov/mimoc/> as well as on a
604 European server. All files are provided in netCDF format, and mixed layer files are
605 additionally available in geotiff format. Each parameter is available as gridded
606 objectively mapped fields and as well as smoother gridded weighted mean fields (see
607 manuscript for description).

608 Global 0–1950 dbar pressure-gridded monthly fields of potential temperature and
609 practical salinity, conservative temperature & absolute salinity, mapped time (in year) of
610 data (see manuscript for description), and the sums of data weights are all available for
611 download.

612 The above parameters are also available on selected isopycnal levels from the
613 bottom of the mixed layer to 1950 dbar, further including the pressures of these
614 isopycnals.

615 Mixed-layer files contain the mixed layer depth (more accurately the maximum
616 mixed layer pressure), and other parameters listed above, as computed by the *Holte et al.*
617 [2009] algorithm and mapped as described in the text.

618 As MIMOC develops, further files and parameters may be added.

619

620 *Acknowledgments.* We thank all those who participated in the collection, calibration, and
621 assembly of the shipboard (http://www.nodc.noaa.gov/OC5/WOD09/pr_wod09.html),
622 Argo, and ITP CTD data used here. The Ice-Tethered Profiler data were collected and
623 made available by the Ice-Tethered Profiler Program based at the Woods Hole
624 Oceanographic Institution (<http://www.whoi.edu/itp>). Argo float profile data were
625 collected and made freely available by the International Argo Project and the national
626 programs that contribute to it (<http://www.argo.ucsd.edu>). We thank Ruth Curry and four
627 anonymous reviewers for their helpful comments on drafts of the manuscript. The
628 research presented in this paper was carried out on the High Performance Computing
629 Cluster supported by the Research and Specialist Computing Support service at the
630 University of East Anglia. The NOAA Climate Program Office and NOAA Research
631 supported this work. PMEL Contribution Number 3805.

632 References

- 633 Amante, C., and B. W. Eakins (2009), *ETOPO1 1 Arc-Minute Global Relief Model:*
634 *Procedures, Data Sources and Analysis*, NOAA Technical Memorandum NESDIS
635 NGDC-24, U.S. Government Printing Office, Washington, D.C., 19 pp.
- 636 Antonov, J. I., D. Seidov, T. P. Boyer, R. A. Locarnini, A. V. Mishonov, H. E. Garcia, O.
637 K. Baranova, M. M. Zweng, and D. R. Johnson (2010), *World Ocean Atlas 2009,*
638 *Volume 2: Salinity*, edited by S. Levitus, NOAA Atlas NESDIS 69, U.S. Government
639 Printing Office, Washington, D.C., 184 pp.
- 640 Bainbridge , A. E. (1976), *GEOSECS Atlantic Expedition.*, Sponsored by International
641 Decade of Ocean Exploration, National Science Foundation, U.S. Government
642 Printing Office, Washington, D.C.
- 643 Boyer, T. P., J. I. Antonov , O. K. Baranova, H. E. Garcia, D. R. Johnson, R. A.
644 Locarnini, A. V. Mishonov, T. D. O'Brien, D. Seidov, I. V. Smolyar, and M. M.
645 Zweng (2009), *World Ocean Database 2009*, edited by S. Levitus, NOAA Atlas
646 NESDIS 66, U.S. Gov. Printing Office, Wash., D.C., 216 pp., DVDs. 2
- 647 Bretherton, F., R. Davis, and C. Fandry (1976), A technique for objective analysis and
648 design of oceanographic experiments applied to MODE-73, *Deep-Sea Res.*, 23, 559–
649 582, doi:10.1016/0011-7471(76)90001-2.
- 650 Cleveland, W. S. (1981), LOWESS: A program for smoothing scatterplots by robust
651 locally weighted regression, *The American Statistician*, 35, 54.
- 652 Coachman, L. K. (1986), Circulation, water masses, and fluxes on the southeastern
653 Bering Sea Shelf, *Cont. Shelf Res.*, 5, 23–108, doi: 10.1016/0278-4343(86)90011-7.

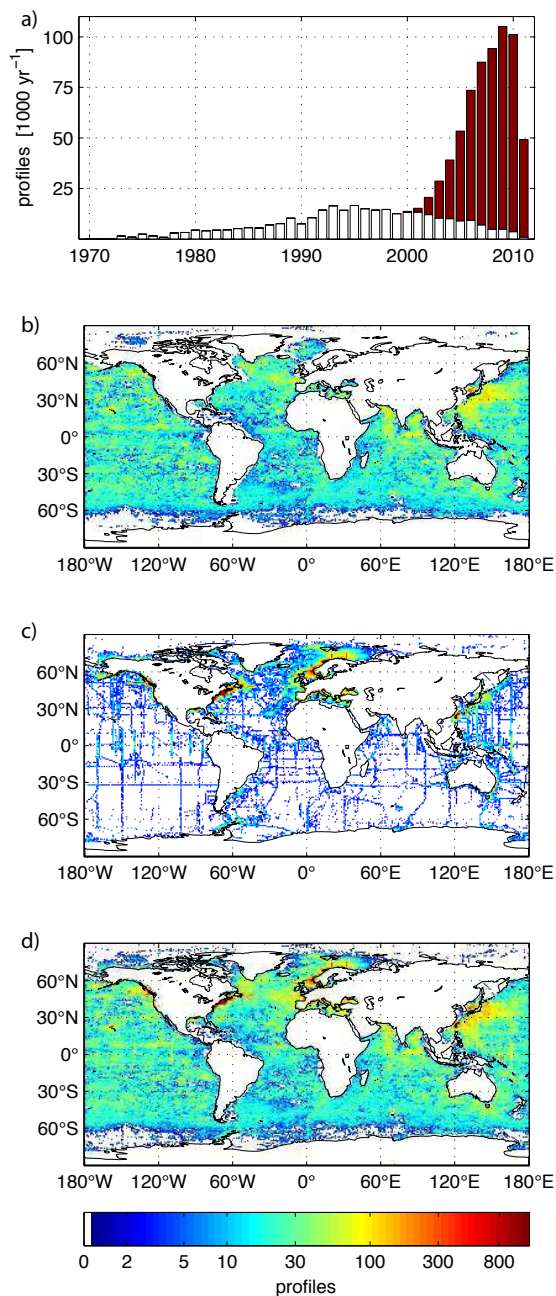
- 654 Curry, R. G. (1996), *HydroBase: A Database of Hydrographic Stations and Tools for*
655 *Climatologic Analysis*, WHOI Technical Report 96-01, 55 pp.
- 656 de Boyer Montégut, C., G. Madec, A. S. Fischer, A. Lazar, and D. Iudicone (2004),
657 Mixed layer depth over the global ocean: an examination of profile data and a profile-
658 based climatology, *J. Geophys. Res.*, *109*, C12003. doi:10.1029/2004JC002378.
- 659 Deacon, G. E. R. (1937), The Hydrology of the Southern Ocean, *Discovery Reports*, *15*,
660 124 pp.
- 661 Dijkstra, E. W. (1959), A note on two problems in connexion with graphs, *Numerische*
662 *Mathematik*, *1*, 269–271, doi:10.1007/BF0138639.
- 663 Flament, P. (2002), A state variable for characterizing water masses and their diffusive
664 stability: spiciness, *Prog. Oceanogr.*, *54*, 493–501, PII S0079-6611(02)00065-4,
665 doi:10.1016/S0079-6611(02)00065-4.
- 666 Fuglister, F. C. (1960), Atlantic Ocean Atlas of Temperature and Salinity Profiles and
667 Data from the International Geophysical Year of 1957–1958, *Woods Hole*
668 *Oceanographic Institution Atlas Series*, *1*, Woods Hole, Massachusetts, 209 pp.
- 669 Gille, S. T. (2004), How nonlinearities in the equation of state of seawater can confound
670 estimates of steric sea level change, *J. Geophys. Res.*, *109*, C03005,
671 doi:10.1029/2003JC002012.
- 672 Gordon, A. L. (1966), Potential temperature, oxygen and circulation of bottom water in
673 the Southern Ocean, *Deep-Sea Res.*, *13*, 1125–1138, doi:10.1016/0011-
674 7471(66)90704-2.
- 675 Gouretski, V., and K. Koltermann (2004), WOCE Global Hydrographic Climatology,
676 *Berichte des BSH*, *35*, 52 pp., ISSN: 0946-6010.

- 677 Helber, R. W., A. B. Kara, J. G. Richman, M. R. Carnes, C. N. Barron, H. E. Hurlburt,
678 and T. Boyer (2012), Temperature versus salinity gradients below the ocean mixed
679 layer, *J. Geophys. Res.*, *117*, C05006, doi:10.1029/2011JC007382.
- 680 Holte, J., and L. Talley (2009), A new algorithm for finding mixed layer depths with
681 applications to Argo data and Subantarctic Mode Water formation, *J. Atmos. Oceanic*
682 *Tech.*, *26*, 1920–1939, doi:10.1175/2009JTECHO543.1.
- 683 Holte, J., J. Gilson, L. Talley and D. Roemmich (2010), Argo Mixed Layers, Scripps
684 Institution of Oceanography/UCSD, <http://mixedlayer.ucsd.edu>, August 2012.
- 685 IOC, SCOR and IAPSO, (2010), The International Thermodynamic Equation of Seawater
686 - 2010: Calculation and Use of Thermodynamic Properties, Intergovernmental
687 Oceanographic Commission, Manuals and Guides No. 56, UNESCO (English), 196
688 pp.
- 689 Johnson, G. C., and M. J. McPhaden (1999), Interior pycnocline flow from the
690 subtropical to the equatorial Pacific Ocean, *J. Phys. Oceanogr.*, *29*, 3073–3089,
691 doi:10.1175/1520-0485(1999)029<3073:IPFFTS>2.0.CO;2.
- 692 Johnson, G. C., B. M. Sloyan, W. S. Kessler, and K. E. McTaggart (2002), Direct
693 measurements of upper ocean currents and water properties across the tropical Pacific
694 Ocean during the 1990's, *Prog. Oceanogr.*, *52*, 31–61, PII S0079-6611(02)00021-6,
695 doi:10.1016/S0079-6611(02)00021-6.
- 696 Johnson, G. C., P. J. Stabeno, and S. D. Riser (2004), The Bering Slope Current System
697 revisited, *J. Phys. Oceanogr.*, *34*, 384–398, doi:10.1175/1520-
698 0485(2004)034<0384:TBSCSR>2.0.CO;2.

- 699 King, B. A., E. Firing, and T. M. Joyce (2001), Shipboard Observations during WOCE in
700 Ocean Circulation and Climate: Observing and Modelling the Global Ocean, edited
701 by G. Siedler et al., International Geophysics, Volume 77, Academic Press, 99–122.
- 702 Klatt, O., O. Boebel, and E. Fahrbach (2007), A profiling float's sense of ice, *J. Atmos.*
703 *Oceanic Tech.*, 24, 1301–1308, doi:10.1175/JTECH2026.1.
- 704 Locarnini, R. A., A. V. Mishonov, J. I. Antonov, T. P. Boyer, H. E. Garcia, O. K.
705 Baranova, M. M. Zweng, and D. R. Johnson (2010), *World Ocean Atlas 2009*,
706 *Volume 1: Temperature*, edited by S. Levitus, NOAA Atlas NESDIS 68, U.S.
707 Government Printing Office, Washington, D.C., 184 pp.
- 708 Lozier, M. S., M. S. McCartney and W. B. Owens (1994), Anomalous anomalies in
709 averaged hydrographic data, *J. Phys. Oceanogr.*, 24, 2624–2638, 10.1175/1520-
710 0485(1994)024<2624:AAIAHD>2.0.CO;2.
- 711 Lozier, M. S., W. B. Owens, and R. G. Curry (1995), The climatology of the North
712 Atlantic, *Prog. Oceanogr.*, 36, 1–44, doi:10.1016/0079-6611(95)00013-5.
- 713 McDougall, T. J. (1987), Thermobaricity, cabbeling, and water-mass conversion, *J.*
714 *Geophys. Res.*, 92, 5448–5464, doi:10.1029/JC092iC05p05448.
- 715 McDougall, T. J., and D. R. Jackett (2005), The material derivative of neutral density, *J.*
716 *Mar. Res.*, 63, 159–185, 10.1357/0022240053693734.
- 717 McDougall T. J., P. M. Barker, R. Feistel and D. R. Jackett (2012), A computationally
718 efficient 48-term expression for the density of seawater in terms of conservative
719 temperature, and related properties of seawater, To be submitted to Journal of
720 Atmospheric and Oceanic Technology.

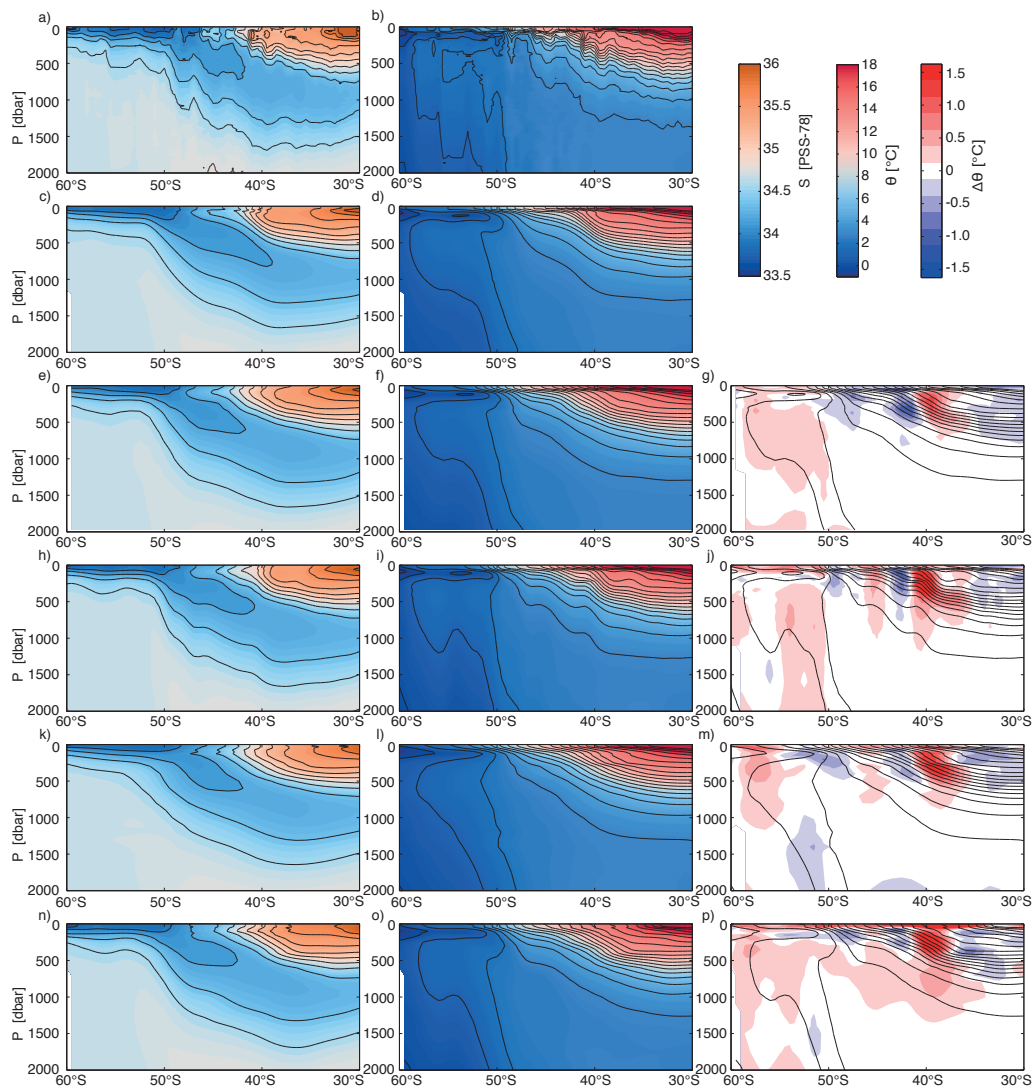
- 721 McPhaden, M. J., and X. Yu (1999), Equatorial waves and the 1997–98 El Niño,
722 *Geophys. Res. Lett.*, 26, 2961–2964, doi:10.1029/1999GL004901.
- 723 Murray J. (1885), A Summary of the Scientific Results, Challenger Reports, 1608 pp.
- 724 Nansen, F. (1900), The Norwegian North Polar Expedition, 1893–1896: Scientific
725 Results, edited by F. Nansen, Pub. by the Fridtjof Nansen Fund for the Advancement
726 of Science. Vol. 1–6.
- 727 Pedlosky, J. (1987), *Geophysical Fluid Dynamics*, Springer-Verlag, New York, 710 pp.
- 728 Pytkowicz, R. M. (1968), Water Masses and their Properties at 160°W in the Southern
729 Ocean, *J. Oceanogr. Soc. Japan*, 24, 1, 21–31.
- 730 Ridgway K. R., J. R. Dunn, and J. L. Wilkin (2002), Ocean interpolation by four-
731 dimensional least squares –Application to the waters around Australia, *J. Atmos.*
732 *Ocean. Tech.*, 19, 1357–1375, doi:10.1175/1520-
733 0426(2002)019<1357:OIBFDW>2.0.CO;2.
- 734 Roemmich, D., and J. Gilson (2009), The 2004–2008 mean and annual cycle of
735 temperature, salinity, and steric height in the global ocean from the Argo Program,
736 *Prog. Oceanogr.*, 82, 81–100, doi:10.1016/j.pocean.2009.03.004.
- 737 Roemmich, D., G. C. Johnson, S. Riser, R. Davis, J. Gilson, W. B. Owens, S. L. Garzoli,
738 C. Schmid, and M. Ignaszewski (2009), The Argo Program: Observing the global
739 ocean with profiling floats, *Oceanogr.*, 22(2), 34–43, doi:10.5670/oceanog.2009.36.
- 740 Rudnick, D. L., and R. Ferrari (1999), Compensation of horizontal temperature and
741 salinity gradients in the ocean mixed layer, *Science*, 283, 526–529,
742 doi:10.1126/science.283.5401.526.

- 743 Schmidtko, S., and G. C. Johnson (2012), Multidecadal warming and shoaling of
744 Antarctic Intermediate Water, *J. Climate*, *25*, 207–221, doi:10.1175/JCLI-D-11-
745 00021.1.
- 746 Sethian, J. A. (1996), A fast marching level set method for monotonically advancing
747 fronts, *Proc. Nat. Acad. Sci.*, *93*, 1591–1595, doi:10.1073/pnas.93.4.1591
- 748 Sethian, J. A. (1999), Fast Marching Methods, *SIAM Review*, *41*, 199–235.
749
- 750 Stommel, H. (1979), Determination of water mass properties of water pumped down
751 from the Ekman layer to the geostrophic flow below, *Proc. Natl. Acad. Sci.*, *76*,
752 3051–3055, doi:10.1073/pnas.76.7.3051.
- 753 Toole, J. M., R. A. Krishfield, M.-L. Timmermans, and A. Proshutinsky (2011), The Ice-
754 Tethered Profiler: Argo of the Arctic, *Oceanogr.*, *24*(3), 126–135,
755 doi:10.5670/oceanog.2011.64.
- 756 Tsuchiya, M., L. D. Talley, and M. S. McCartney (1994), Water-mass distributions in the
757 western South Atlantic; A section from South Georgia Island (54S) northward across
758 the equator, *J. Mar. Res.*, *52*, 55–81, doi:10.1357/0022240943076759.
- 759 Wong, A. P. S., and G. C. Johnson (2003), South Pacific Eastern Subtropical Mode
760 water, *J. Phys. Oceanogr.*, *33*, 1493–1509, doi:10.1175/1520-
761 0485(2003)033<1493:SPESMW>2.0.CO;2.
- 762 Wüst, G., and A. Defant (1936), Schichtung und Zirkulation des Atlantischen Ozeans.
763 *Wiss. Ergebn. Dt. Atlant. Exped. "Meteor" 1925–1927, Bd. VI, Atlas, 103pp.*



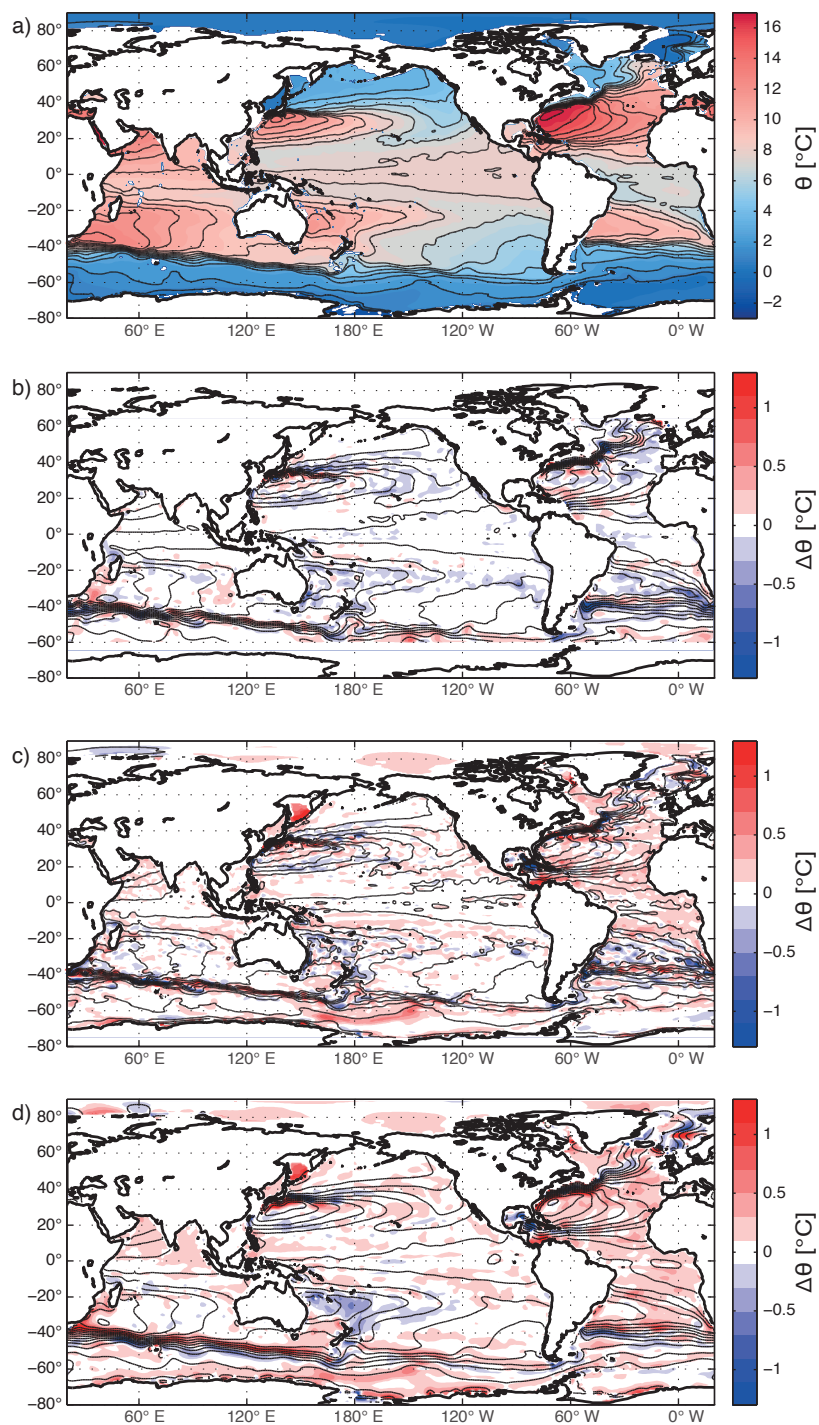
764

765 Figure 1. Data distribution for MIMOC. (a) Temporal distribution of CTD profiles from
 766 WOD (white) and Argo/ITP profiles (red). (b) Spatial distribution of Argo and reduced
 767 ITP profiles (see text) for each 1°x1° grid box in logarithmic colors. (c) Similar to (b),
 768 but for WOD profiles. (d) Similar to (b), but for Argo, reduced ITP, and WOD profiles
 769 combined.



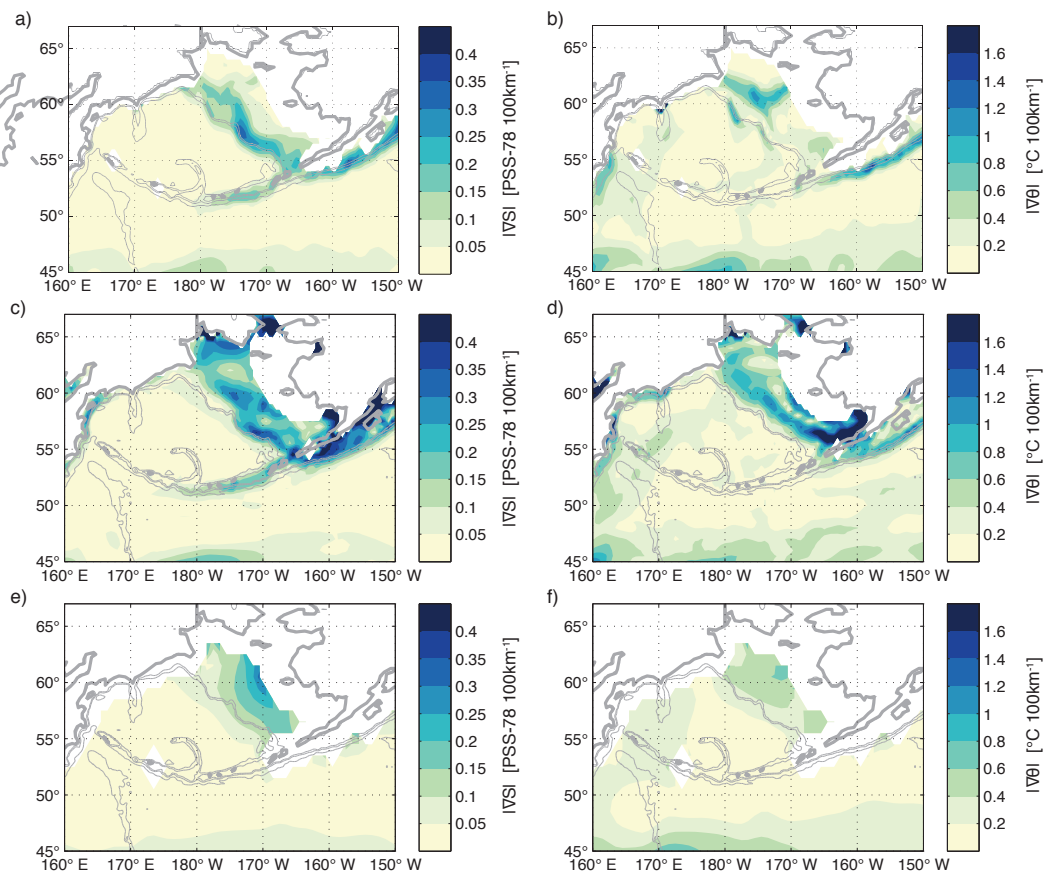
770

771 Figure 2. Meridional-vertical sections of (a) salinity (S) and (b) potential temperature (θ)
 772 for WOCE A16S in the western South Atlantic Ocean Jan.–Feb. 2005 (e.g., Johnson and
 773 Doney 2006). Corresponding MIMOC sections for (c–d) θ and S in January along
 774 32.5°W . Similarly for (e–f) AMA and (g) MIMOC minus AMA θ (colors). Similarly for
 775 (h–j) CARS09, (k–m) WOA09, and WGHC (n–p), with WGHC being an annual mean.
 776 Isohalines are contoured at 0.2 intervals and isotherms at 1°C intervals for each
 777 climatology and the synoptic data (black lines).



778

779 Figure 3. Maps of (a) MIMOC θ at 500 dbar in May and differences (MIMOC – each
 780 climatology) in color for (b) AMA, (c) CARS09, and (d) WOA09. Isotherms for each
 781 climatology are contoured at 1°C intervals (black lines).



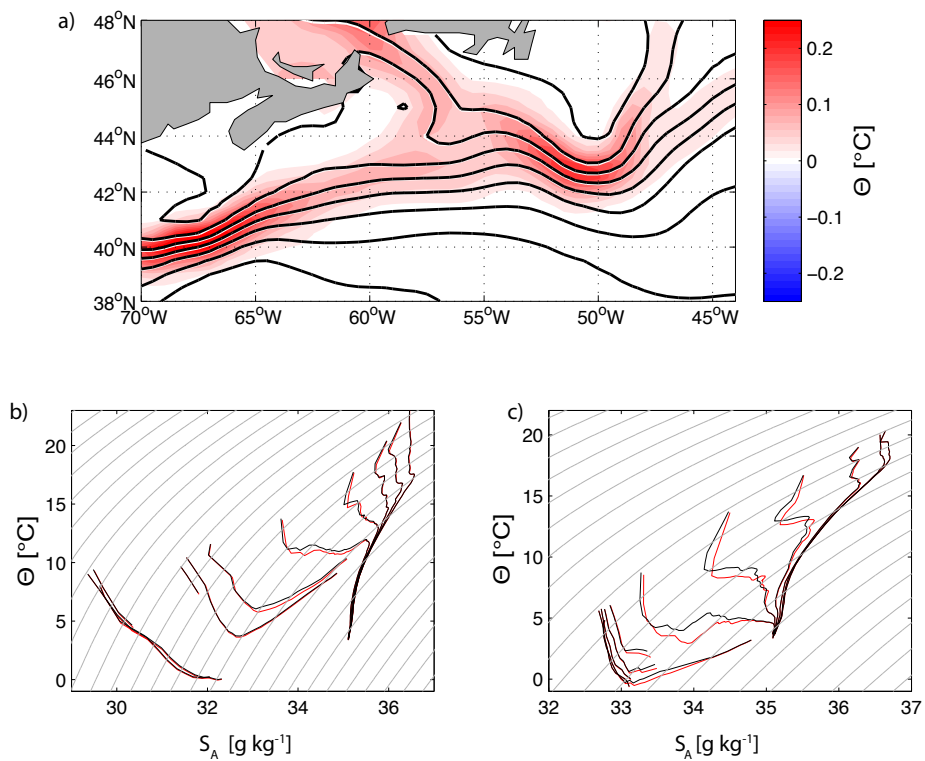
782

783 Figure 4. Maps of S (left panels) and θ (right panels) gradients at 50 dbar in the Bering

784 Sea and Shelf for (a–b) MIMOC, (c–d) CARS09 (c-d), and (e–f) WOA09. The coast

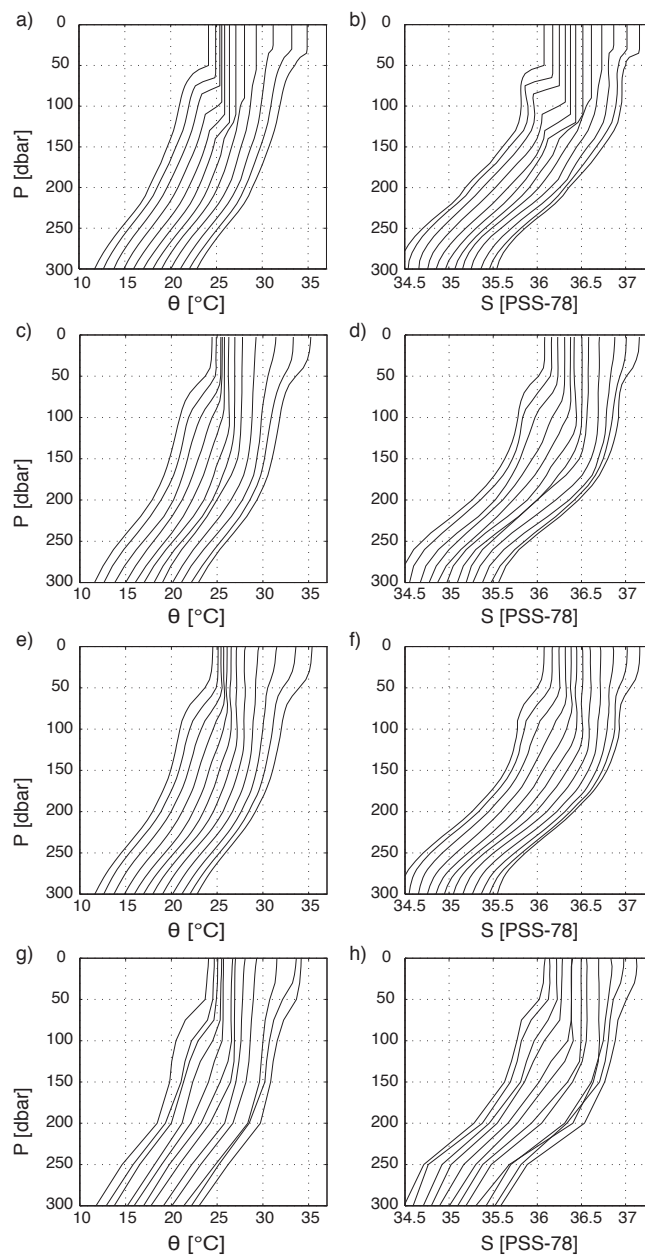
785 (thick grey lines) and 1000, 2000, and 3000-m isobaths (thin grey lines) are shown. The

786 AMA climatology is omitted since it does not cover the Bering Sea or Shelf.



793

794 Figure 6. Map of (a) June conservative temperature (Θ) cabelling corrections in mixed
 795 layer of the North Atlantic Current (color), isotherms contoured at 2°C intervals, in the
 796 (white) uncorrected and (black) corrected/adjusted data set. Sets of Θ - S_A curves at 1° lat.
 797 intervals for June over the upper 1500 dbar at (b) 62.5°W and (c) 49.5°W showing
 798 uncorrected (red) and corrected (black) values.



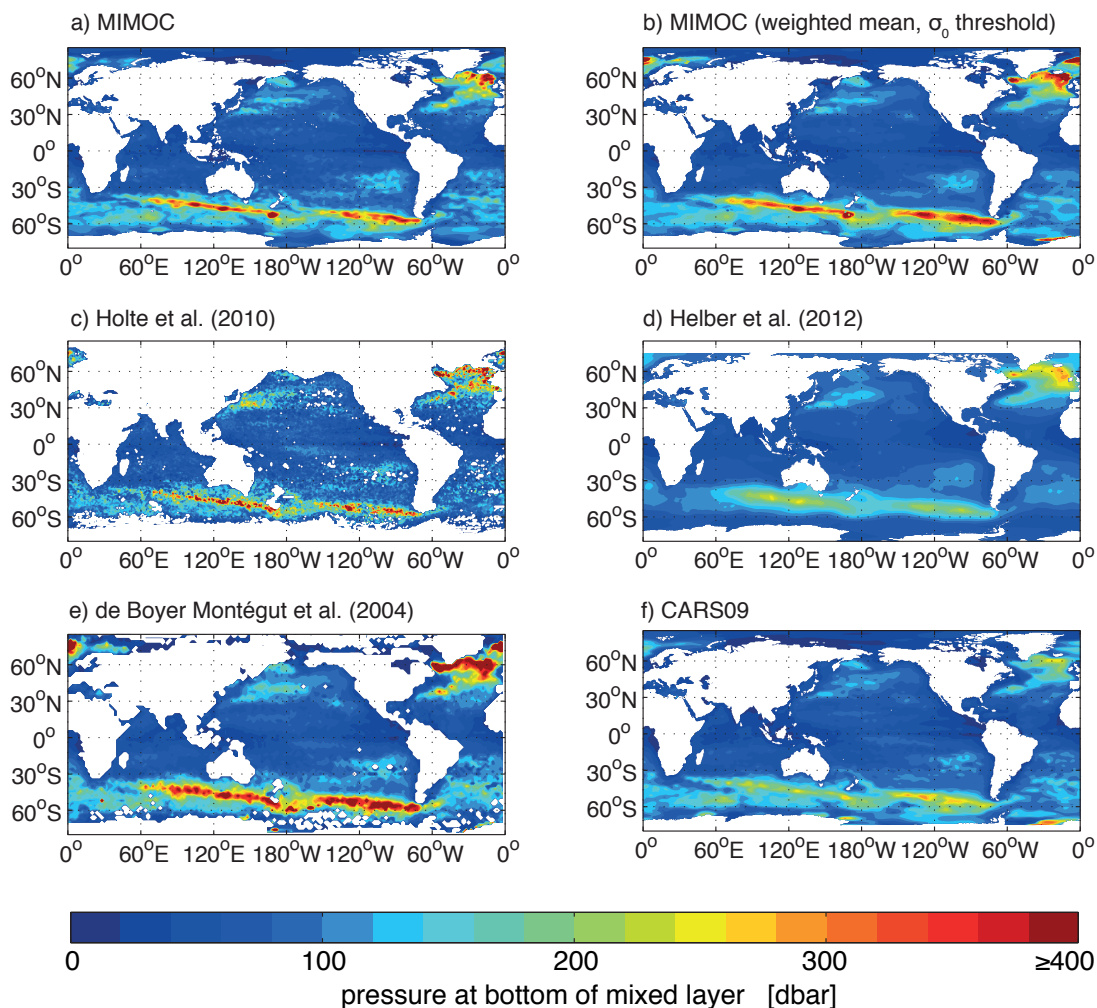
799

800 Figure 7. Temporal evolution over 12 months in the SEPSTMW formation region

801 (20.5°S 99.5°W) starting with the lightest ML in March for (a) θ and (b) S in MIMOC

802 offset by 1°C and 0.1 PSS-78 per month, respectively. Similarly for (c-d) AMA, (e-f)

803 CARS09, and (g-h) WOA09.



804

805

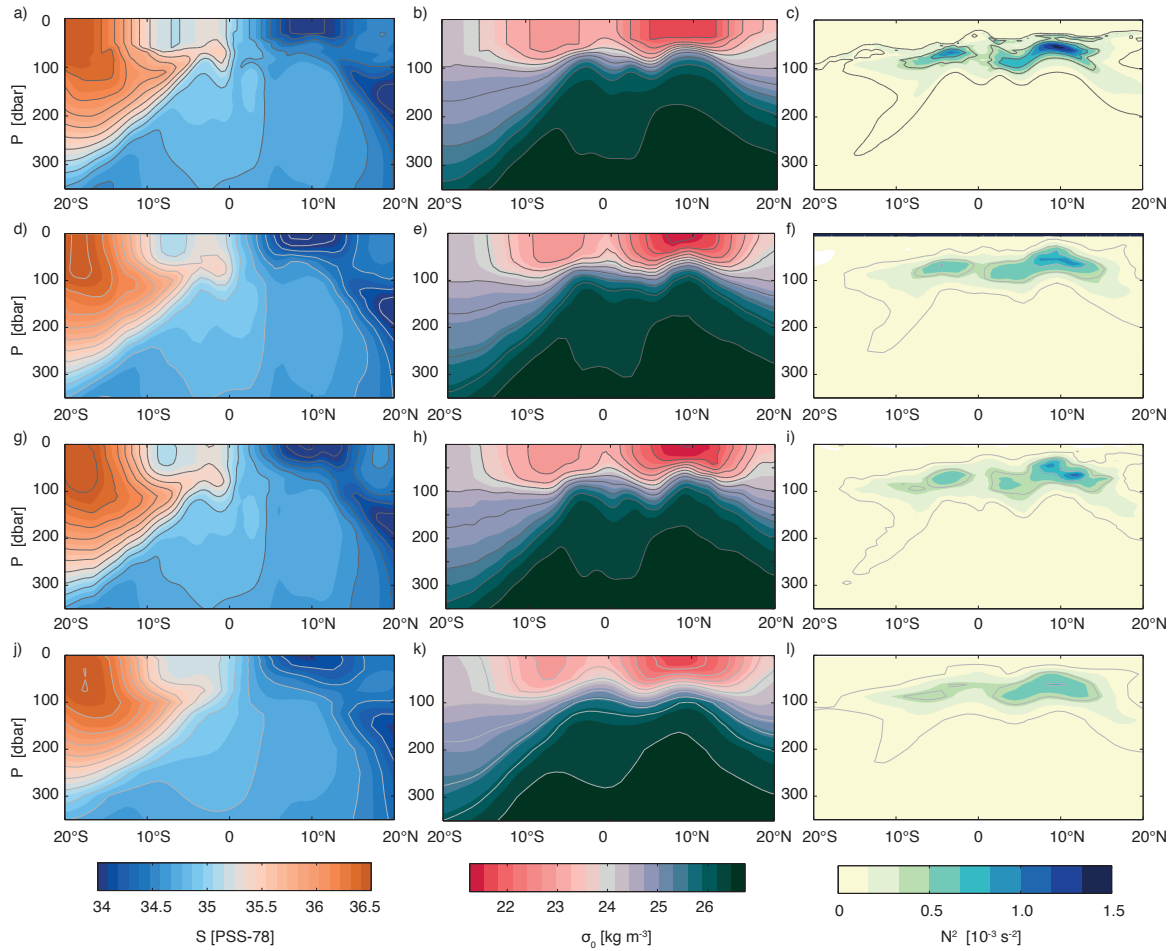
806 Figure 8. Maximum annual mixed layer depth from different climatologies. a) MIMOC

807 objective analysis of MLP determined by the *Holte et al.* [2009] density algorithm for

808 individual profiles, b) MIMOC weighted mean analysis MLP with density threshold of

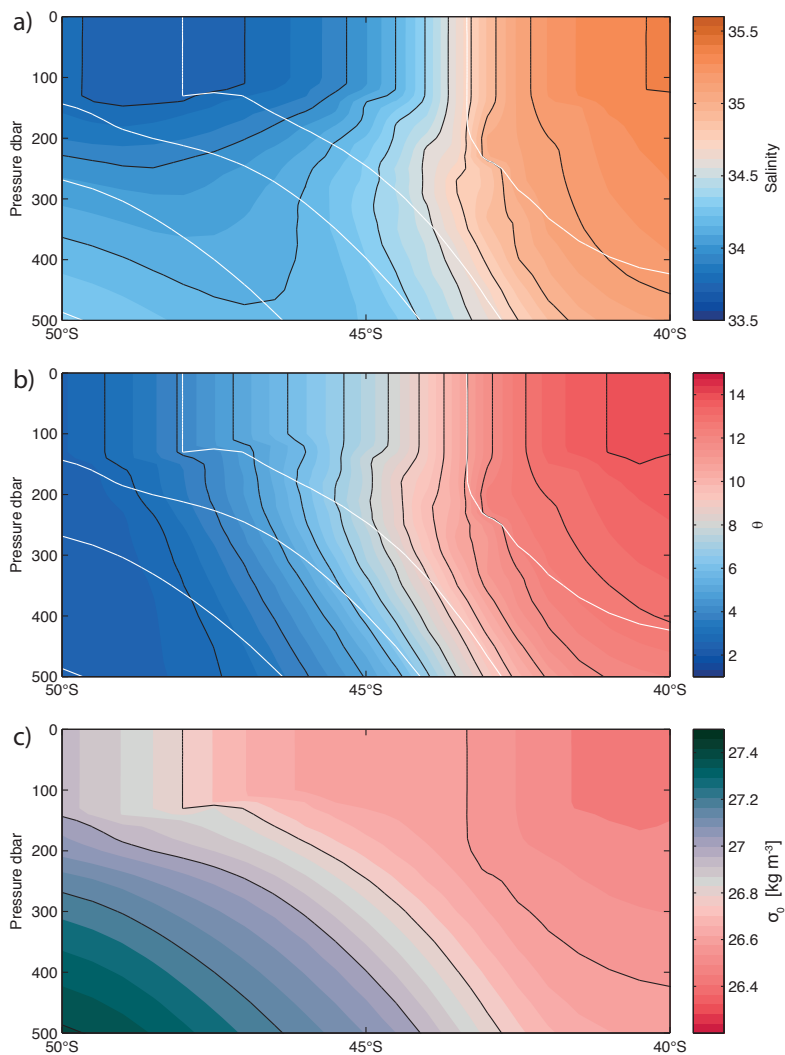
809 0.03 kg m^{-3} , c) *Holte et al.* [2010] maximum recorded MLP by density algorithm within810 $1^\circ \times 1^\circ$ bin, d) *Helber et al.* [2012] maps, e) *de Boyer Montégut et al.* [2004] temperature

811 threshold f) CARS09 values.



812

813 Figure 9. Meridional-vertical sections across the equatorial Pacific along 119.5°W in
 814 October, of S (left panels), σ_0 (central panels) and Brunt-Väisälä frequency squared, N^2 ,
 815 (right panels) for (a–c) MIMOC, (d–f) AMA, (g–i) CARS09, and (j–l) WOA09.
 816 Isohalines are contoured at 0.2 PSS-78 intervals, isopycnals at 0.5 kg m^{-3} intervals and
 817 isolines of N^2 at $0.3 \cdot 10^{-3} \text{ s}^{-2}$ intervals starting at $0.1 \cdot 10^{-3} \text{ s}^{-2}$. AMA maps for individual
 818 Octobers have a stronger pycnocline than the multi-October average shown here.



819

820 Figure 10. Meridional-vertical sections of MIMOC (a) S , (b) θ , and (c) σ_{θ} along 60.5°E in

821 September across the Antarctic Circumpolar Current. Isohalines are contoured at 0.2

822 PSS-78 intervals, isotherms at 1°C intervals in their respective panels (black lines) and823 potential isopycnals (white lines in (a) and (b), black lines in (c)) at 0.2 kg m^{-3} intervals.

824 TABLE 1. Parameters of climatologies compared in this study.

	Climatology name			
	WOA09	CARS09	AMA	MIMOC
Mapping surfaces	isobaric	isobaric	isobaric	isopycnal & mixed layer
Vertical level count (to 1950 dbar ¹)	40 (24)	79 (65)	58 (57)	81 (81) ²
Horizontal resolution	1°x1°	0.5°x0.5°	0.5°x0.5°	0.5°x0.5°
Max. depth (with seasonal cycle)	5500 m (1500 m)	5500 dbar (1800 dbar ³)	1975 dbar (1975 dbar)	1950 dbar (1950 dbar)
Mapping method	multi-pass Gaussian smoothing	LOESS	objective analysis	objective analysis
Covariance shape, bathymetry influence on mapping	circular, regional boundaries between basins	CSIRO-BAR filter (ellipse along bathymetry)	distance penalty for profiles over varying topography	path finding algorithm using median filtered ETOPO-1
Mixed layer	none, separate climatology available	none, separate climatology available	none	included, separate climatology available
Variables mapped	T , S , & biogeochemical	T , S , & limited biogeochemical	T & S	θ & S , Θ & S_A

825 ¹WOA09 uses depth for the vertical coordinate, so 1950 m is used as its break point.826 ²Also available for the mixed layer and on selected isopycnal surfaces.827 ³Mean, annual, and semi-annual harmonics from 0–1000 dbar, mean and annual

828 harmonics from 1000-1800 dbar, mean only below 1800 dbar.